

Improving Resolution and Resolvability of Single Particle CryoEM using Gaussian Mixture Models

Muyuan Chen^{1*}, Michael F. Schmid¹, Wah Chiu^{1,2}

¹ Division of CryoEM and Bioimaging, SSRL, SLAC National Accelerator Laboratory, Stanford University, Menlo Park, CA 94025, USA

² Department of Bioengineering, and of Microbiology and Immunology, Stanford University, Stanford, CA 94305, USA

* Correspondence to: muyuanc@stanford.edu

Abstract

Cryogenic electron microscopy is widely used in structural biology, but the resolution it achieves is often limited by the dynamics of the macromolecule. Here, we developed a refinement protocol based on Gaussian mixture models that integrate particle orientation and conformation estimation, and improves the alignment for flexible domains of protein structures. We demonstrated this protocol on multiple datasets, resulting in improved resolution and resolvability by visual and quantitative measures.

Main

Single particle cryogenic electron microscopy (CryoEM) is a technique that leverages information from multiple independent observations of the same protein at different orientations to reconstruct its structure in 3D. This method can now determine rigid protein structures at atomic resolution¹⁻⁴, and the number of near-atomic resolution CryoEM structures deposited in the Protein Data Bank continues to rise. In order to reconstruct the 3D structure, the orientation of 2D particles images are determined computationally, typically by iteratively searching for the optimal pose (rotation-translation parameters) that maximizes the similarity between each particle image and the projection of the 3D density map^{5,6}.

To estimate the pose of particles, algorithms assume that the 2D images represent observations of the same 3D structure at different orientations. However, this assumption becomes invalid when the macromolecule has compositional or conformational heterogeneity, leading to

limitations in the resolution achieved by CryoEM. To overcome this issue, various computational methods have been developed. Focused and multibody refinement addresses heterogeneity by refining particle orientation for individual domains after density subtraction, but the alignment can be affected by artifacts from masking and subtraction⁷. Machine learning-based manifold embedding methods have been proposed to address protein flexibility by learning the conformational changes from particle images^{8,9}. However, it remains challenging to obtain high-resolution reconstructions for the flexible regions, because the signal to noise ratio (SNR) is often limited by the number of particles at the exact same conformation along a continuous movement trajectory. While the learned conformational changes can sometimes be used to generate deformed structures with improved features^{10,11}, those maps are different from direct reconstruction from particles, which are free from potential deformation artifacts and may contain features invisible in the consensus map.

Recently, we have developed a protocol that uses Gaussian mixture models (GMMs) instead of voxel maps for structure representation, and extract movement trajectories of proteins directly from the particles using deep neural networks (DNN) techniques¹². To further improve the resolution and resolvability, we expanded the GMM-based refinement workflow, which now optimizes the orientation of particles in addition to their conformations (**Fig.S1**). Using the technique, the knowledge of conformational heterogeneity can be transferred to orientation of particles, to better resolve the domains undergoing large-scale continuous movement.

For GMM-based orientation refinement, the protocol starts with a homogeneous refinement and uses existing pose estimations provided by voxel-based methods using software such as EMAN2, Relion, and CryoSparc^{5,6,13}. To prevent overfitting, the “gold-standard” even/odd particle split is kept throughout the entire process, and one GMM is built from the density map of each subset. In each iteration, the pose of particles are locally refined using the Adam optimizer¹⁴, and 3D reconstructions are computed from the particle images with new orientations using direct Fourier inversion. The usage of GMM brings a number of advantages. First, compared to the voxel maps, the GMMs require only ~1% of variables to represent the same structure¹⁵, which reduces the computational cost and increases the observation/variable ratio. Second, as we only project the Gaussian coordinates to generate Fourier images, no interpolation is needed throughout the alignment. Third, since central Gaussian coordinates are located on protein densities, the GMM essentially provides a tight mask around the molecule without creating artifacts in real or Fourier space. Finally, because the GMM is a continuous function in 3D, the optimization can take

advantage of accurate gradients calculated using deep learning packages¹⁶. All these features are particularly helpful for resolving smaller macromolecules at high resolution, where the SNR is low and the artifacts from interpolation and masking have a strong impact on alignment.

Next, we implement GMM-based focused refinement. With GMMs, we can adjust not only the amplitude, but also the width of Gaussian functions within a target region. Since Gaussian width is equivalent to the local resolvability, by using GMM references with increased width outside the region, the alignment focuses on high-resolution features within the region, while still being constrained by the low-resolution information throughout the entire structure. Furthermore, we can use a patch-by-patch refinement strategy to improve the resolvability of the entire macromolecule. That is, we segment the full GMM into multiple patches, focus refine each individual one, then merge the results together into a final composite map.

Finally, we integrate the pose estimation with the previously developed heterogeneity analysis¹². The process starts from the DNN-based heterogeneity analysis using the orientation assignment from the GMM-based consensus refinement. After the heterogeneity analysis, the trained decoder outputs one GMM for each point from the latent space, corresponding to the conformation of that particle. While the overall movement within a protein can be complex, we assume that within a small enough local region, the structure moves as a rigid body. Therefore, we can change the reference frame of the movement to focus the alignment on the target domain. For each particle, we search for the optimal pose that minimizes the difference within the region between the GMM of the conformational state of that particle, and the neutral state GMM at the initial orientation. Reconstruction of all particles at the new orientation will have better-resolved features at the target region, and smeared-out densities in the rest of the structure. A few rounds of focused refinement are then performed starting from this Euler angle assignment to further improve the resolvability of that region.

To demonstrate the performance of the method, we tested it on three datasets. To make a fair comparison, we selected public datasets with assigned particle orientations provided by the authors. In all examples, the same particles, masking, and structure sharpening were used, to ensure the only difference between the results comes from the orientation assignment.

We started from a relatively rigid GPCR dataset from EMPIAR-10786¹⁷. The “gold-standard” resolution of the initial structure was 3.3Å, which was improved to 2.5Å after GMM-based patch-

by-patch refinement. As a measure of resolvability, average Q-score¹⁸ increased from 0.60 to 0.67. The GMM-based refinement led to improved real space features across the entire density map. At the nanobody, β -strands are better separated and previously unmodeled broken density becomes connected. Along the ECL at the opposite side of the protein, we also observed better backbone connectivity and sidechain density (**Fig.1A-D, Fig.S2, Supplementary movie 1**).

Next, we demonstrated focused refinement on a SARS-COV2 spike dataset (EMPIAR-10492)¹⁹. In this dataset, the lower parts of the spike are well resolved, whereas the upper parts, including the RBD and the NTD are more flexible. Here, we improved “gold-standard” resolution from 3.8Å to 3.1Å, and the average Q-score from 0.47 to 0.53. The refinement also greatly improved features at the flexible domains. Strands in β -sheets become clearly separable, and sidechains start to show up in the refined structure (**Fig.1E-H, Fig.S3, Supplementary movie 2**).

In the third example, we show the integration with the DNN-based heterogeneity analysis using an ABC transporter dataset (EMPIAR-10374)²⁰. This structure contains rigid TMDs, flexible NBDs, and Fabs that are undergoing large-scale movement and are blurred out in the consensus map. The GMM-based refinement increased “gold-standard” resolution from 3.2Å to 2.8Å. Focused refinement improved the resolvability of the NBD, but its performance on the Fab was suboptimal. So, we ran the DNN-based heterogeneity analysis focusing on one of the Fabs, which showed a continuous tilting movement of as much as 14Å. Then, the conformations of particles were converted to the change of pose at the region, and a few rounds of focused refinement were performed afterwards. The refinement yielded clear high-resolution features at the Fab, including separable β -strands with sidechains. Combining with patch-by-patch refinement results for the rest of the protein, the overall resolution reached 2.5Å (**Fig.2, Fig.S4, Supplementary movie 3, 4**).

In summary, by refining particle orientation using GMMs instead of voxel maps as references, we obtain reconstructions with higher “gold-standard” resolution and better resolved real-space features. The usage of GMMs also makes it easier to focus the alignment on local regions, and by segmenting the GMM into patches and focusing on every patch individually, we can further improve the resolution and resolvability of features throughout the structure. Combined with the DNN-based heterogeneity analysis, information of conformational changes can be converted to particle orientations, leading to greatly improved features at the highly flexible protein domains

that are undergoing continuous motion. The method is compatible with most CryoEM software packages, and shows superior performance on a wide range of macromolecules.

Methods

Construction of Gaussian model

The first step in constructing the GMM is to determine the number of Gaussians (N) in the model. The recent improvement of the GMM implementation makes it possible to represent the macromolecule with tens of thousands of Gaussian functions within the capability of modern GPUs¹⁵. So, when the sequence is known and the target resolution is 3Å or higher, it is convenient to simply set N to be the number of non-H atoms in the molecule. In our experience, small changes (10%) of N does not have a significant impact on the result of the refinement. For reconstruction at lower resolution, we also provide tools to automatically estimate the necessary number of Gaussian based on the size of protein and target resolution. Essentially, this is done by building GMMs of variable N on the same map, and searching for an optimal N so that the average nearest neighbor distance of the GMM matches the target resolution.

There are two ways to initialize the location of Gaussian functions in the GMM. First, when an existing molecular model is provided, we can take the coordinates from the PDB file, and seed one Gaussian per non-H atom. To avoid overfitting, the coordinates of each Gaussian in the GMM is randomized at the determined gold-standard resolution before being used as references for the even/odd subsets. Alternatively, the initial location of Gaussian functions is determined by clustering voxels in the given density map with values above a given threshold using the K-means algorithm. Empirically, the two initialization methods cause little difference in the results of particle orientation refinement. In our experiments, the two methods yield overlapping FSC curves and virtually identical real space features after the refinement. However, there are some points of concern when choosing the initialization method. Seeding the GMM with a molecular model can lead to broken density in the reconstruction when the given model contains large unmodeled parts that exist in the structure. On the other hand, seeding the GMM using the clustering method can lead to under-representation of the target molecule when there is significant non-target density in the reconstruction, e.g., lipid density in a membrane protein. This can be solved by either masking the density out before seeding the GMM, or increasing the number of Gaussian in the model. In all examples shown in the paper, to avoid model bias, the GMMs are initialized directly from the voxel map, without the information of the existing PDB model.

After initializing the coordinates of Gaussian functions, we initialize the amplitude and width for each Gaussian as constant values. The GMM is then optimized to match the voxel density map, using the same DNN-based procedure described in our previous paper¹². Basically, this is done by maximizing the Fourier ring correlation (FRC) between the projections of the GMM and the density map at different orientations using stochastic gradient descent. All parameters, including coordinates, amplitude and width will be optimized at this step to match the GMM to the consensus density map, typically with an average FSC greater than 0.9 at the target resolution range.

Particle orientation refinement

To refine the orientation of particles, we search for the best Euler angles and translation for each particle, so that the FRC between the particle image and the projection of the GMM is maximized. The particles are phase-flipped as a part of preprocess, and the FRC is normalized by Fourier ring, so we do not have to consider the impact of CTF in the comparison. To project the GMM, we first project the central coordinates of the Gaussian functions, then generate the image of the projected GMM directly in Fourier space in the coordinate system of the particle. Since the GMM is continuous in 3D, no interpolation is required in the process. The orientation search is performed using gradient descent, where the gradient is computed by the automatic differentiation in Tensorflow. After orientation refinement, 3D density maps are reconstructed from the particles using the newly determined Euler angles, which will be used as references to construct the GMMs for the next iteration of refinement.

For focused refinement, we apply the mask to the width of Gaussian in the GMM. For a mask with values between 0 and 1, we use $1/(0.25 + 0.75 M_{x,y,z})$ as the multiplier for the width of a Gaussian function centered at (x, y, z) , where $M_{x,y,z}$ is the value of the given mask at that point. Note that here we increase the width of Gaussian outside the mask, in contrast to an amplitude mask which decreases the Gaussian amplitude outside, since larger width corresponds to lower local resolution. Similar to the classical amplitude mask, the width mask is applied to the GMM after it is trained to match the reconstructed 3D density map at each iteration.

To perform patch-by-patch alignment, we divide the GMM into multiple patches using the K-means clustering algorithm. For each cluster, we create a spherical mask that covers the center of all Gaussian functions in the cluster. Focused refinement is then performed using the spherical

mask. Finally, we combine the results together by multiplying each focused refinement result with its corresponding mask, and generating a weighted average of those density maps using the masks as weights.

Converting conformation to orientation

After the GMM-DNN based heterogeneity analysis, we generate one GMM for each particle by feeding its location in the latent space to the trained decoder. Then, to convert the conformation information to particle orientation, under a given mask of the target region, for each particle, we search for a new angle that minimizes:

$$RMSD((Project(GMM_{neutral}, \theta_{init}) - Project(GMM_{conf}, \theta_{new})) \cdot mask)$$

Here, $Project(GMM, \theta)$ makes the projection of a 3D GMM to 2D at the Euler angle θ . $GMM_{neutral}$ is the GMM built from the consensus refinement, and GMM_{conf} is the GMM at the conformation of that particle. θ_{init} is the initial orientation assignment of the particle, and θ_{new} is the new Euler angle to be optimized. The region of focus is indicated by $mask$, which is a vector with length of the number of Gaussian functions in the GMM. The $mask_i$ is 1 if the i th Gaussian falls within the target region, and 0 if outside the region. Root Mean Square Deviation (RMSD) is used to measure the difference between the two GMMs.

The optimization is also done using the Adam optimizer through Tensorflow, starting from the initially assigned angle for each particle ($\theta_{new} = \theta_{init}$). Afterwards, we reconstruct the particles at the new orientation, and perform multiple iterations of focused refinement with the same mask. To avoid overfitting, the heterogeneity analysis is done for the even/odd particle subsets independently, with one pair of encoder-decoders built for each subset. While the latent spaces produced by the two encoders do not necessarily match, as long as the two neutral state GMMs are aligned to each other, the reconstructions of particles at the converted orientation will still be aligned. Similar to the focused refinement, this process can also be performed separately using different focusing masks, and the results can be merged to produce reconstructions with better features globally.

Structure comparison

For each dataset, we start from importing the extracted particle sets from EMPIAR provided by the authors. First, CTF correction is done by phase flipping each particle according to the

information in the corresponding metadata (Relion star file)⁵. The Euler angles, 2D translation, and the “gold-standard” subset assignment of the particles are also extracted from the metadata, to use as the starting point of the GMM-based refinement. 3D reconstruction is performed using direct Fourier inversion from the particles at their assigned orientations. To ensure the conversion is correct, a script is also provided that can convert the Euler angle GMM-based refinement back to the star file. The metadata can then be converted to the format of CryoSPARC or other software using the Pyem package²¹. Reconstructions in the other software packages using the GMM-refined Euler angles also show improved FSC curves and real space features.

One soft mask is created for each dataset and used for the “gold-standard” FSC calculation. To avoid masking induced artifacts when comparing the FSC measurement, masks used here are often not as tight as the ones used in the original publications, leading to slightly lower resolution numbers than reported. However, real space features are essentially identical since the maps are filtered by their gold-standard resolution locally.

To ensure the real space features between different maps are comparable, we use the same sharpening method for all datasets. For each structure, we simulate a density map from the corresponding molecular model provided by the authors at 2Å, then compute the radial Fourier amplitude profile of the simulated map. The amplitude profile is used to sharpen the reconstructions before they are lowpass filtered to the determined resolution.

The final density maps are lowpass filtered to their gold-standard resolution locally using the method implemented in EMAN2²². The corresponding molecular model from the original publication is fitted to the density map, and automated real space refinement protocol from Phenix is used to optimize the model to fit into the refined map locally²³. Finally, Q-score is computed using the real space refined model and the map, and the averaged Q-score per residue, smoothed over a 11 residue window¹⁸, is reported in the figures. For the local feature comparison, we choose regions with the largest difference between the Q-score from the initial and refined reconstructions. Display of 3D volumes is done in UCSF Chimera and ChimeraX^{24,25}.

Detail on datasets

For the GPCR dataset, we use picked particles of the P-Neurokinin Receptor G protein complexes from EMPIAR-10786¹⁷. Specifically, the reconstruction and final Euler angle assignment of the

SP-NK1R-miniGs399 is used. The dataset includes 288,659 particles with a pixel size of 0.86Å. According to the original publication, the orientation assignment uses a combination of Relion, CryoSPARC and CisTEM. The GMM is seeded on the protein density only, excluding the lipid shell, and the FSC is evaluated using a larger soft mask that includes both the protein and lipid density. 7374 Gaussian functions are included in the GMM, which is the number of non-H atoms in the corresponding molecular model. The “gold-standard” resolution of the initial structure was 3.3Å, which was improved to 2.8Å after the GMM-based global refinement, and 2.5Å after patch-by-patch refinement. The molecular model (PDB: 7RMH) corresponding to the EMPIAR entry was fitted into the density map using Phenix real space refinement against the final density map from the patch-by-patch refinement.

For the dataset of SARS-COV2, we use picked particles from EMPIAR-10492¹⁹, which includes 29,180 particles with their corresponding metadata. The original Euler angle assignment was performed using Relion. Here, since the resolution is lower, we use a GMM of 17,000 Gaussian functions. The number of Gaussian is estimated so that the GMM matches the density map at the target resolution range. The pixel size of the particles is 1.061Å, and the structure is determined with c3 symmetry. The symmetry is expanded to c1 for the focused refinement by duplicating each particle three times at the three symmetrical orientations, and the mask for the refinement covers the target domain of one asymmetrical unit. To generate the final composite map, we reimpose the c3 symmetry to the focused refinement results by weighted average, using the focus masks as weights, then merge the maps from different focused refinement together using the same technique. The “gold-standard” resolution of the initial structure was 3.8Å, which was improved to 3.4Å after the GMM-based global refinement, and 3.1Å after patch-by-patch refinement. The molecular model (PDB: 6ZWV) was fitted into the density map using Phenix real space refinement against the result of patch-by-patch refinement.

The ABC transporter dataset comes from EMPIAR-10374²⁰, a human ABCG2 transporter with inhibitor MZ29 and 5D3-Fab. The dataset contains 284,831 particles with a pixel size of 0.84Å, and the initial orientation is determined using a combination of CryoSPARC and Relion. The GMM includes 15,174 Gaussian functions, the same as the number of non-H atoms in the corresponding molecular model. The Euler angles from Refine3d_C2 are used as the initial particle orientation assignment, and the refinement is performed with c2 symmetry. Similar to the SARS-COV2 dataset, the symmetry is expanded for heterogeneity analysis and focused refinement, then reimposed to generate the final composite map. The GMM-DNN based

heterogeneity analysis is performed focusing on the Fab, using a hierarchical GMM¹⁵ and target 5Å resolution. The molecular models of different conformations (shown in Fig.2B) are generated by morphing the neutral state molecular model (PDB: 6ETI) using the decoder trained from the particles. Since the C-domain of the Fab is not modeled in the original publication, we use an existing Fab structure (PDB: 7FAB), rigid-body fitted to the density map, then optimized to match the final composite map using Phenix real space refinement. The length of the movement trajectory is measured at the residue with the longest movement distance, specifically 205K of the heavy chain. The average Q-score improves from 0.62 to 0.63 after the GMM-based global refinement, and 0.65 after we merge the patches together. Note that the resolvability of the Fab C-domain is not reflected in the Q-score in Fig.S4, due to the difficulty of fitting the molecular model into the original density map reliably to make a fair comparison.

Computational resource consumption

The alignment protocol is implemented using Tensorflow¹⁶, and runs on GPUs with CUDA capability. In our tests, for the refinement of 400,000 particles with box size of 196 pixels and targeting 3Å resolution, one iteration of refinement takes ~2 hours on a Nvidia RTX A5000 GPU. For all examples shown in the paper, five iterations of refinement are sufficient to reach convergence by the FSC measurement. I.e., the “gold-standard” FSC curves do not show clear improvement from the 4th to the 5th iteration. Focused refinement has virtually the same time and resource cost as the refinement of the full protein, and the time consumption of patch-by-patch alignment is N times the focused refinement, where N is the number of patches.

During the refinement of the GPCR dataset, which uses a GMM of 7374 Gaussian functions and a box size of 240, the peak GPU memory use is 8.7GB. In contrast, the peak memory usage during the refinement of the ABC transporter, which uses a GMM with 15,174 Gaussian functions and particles with box size of 256 pixels, is 17.1GB. Note that the GPU memory usage is roughly linear to the batch size used during the refinement, i.e., the number of particles loaded into the GPU memory at the same time, which is set to 16 by default and can be adjusted by users. Different from the training of DNNs, here the orientation of each particle is independent, and we do not need to consider the statistical power for each batch, so this number can be adjusted to balance the speed and GPU memory consumption. I.e., using a batch size of 8 will save about half of the GPU memory in exchange for longer runtime, but the refinement results will not be affected.

The CPU memory consumption during the refinement is also adjustable. By default, 20,000 particles are loaded into the CPU memory each time through the process, which can be changed through program options. However, unlike the batch size that affects the parallelism in GPUs, loading fewer particles into the CPU each time reduces the CPU memory cost but does not significantly slow down the process.

Interpretation of FSC curves

During the comparison of the structures, it is worth noting that the patch-by-patch refinement sometimes contributes less than expected to the global “gold-standard” FSC curves. For example, in the SARS-COV2 spike example (Fig. S3), the patch-by-patch refinement is performed on the top of the GMM-based global alignment, and improves the structure in virtually every aspect. This includes better local resolution throughout the protein, equal or higher Q-score for every residue, and improved real space features. However, the improvement of the overall FSC from the patch-by-patch refinement is relatively small, particularly when compared to the improvement from the original orientation assignment to the result from the global GMM-based refinement. To solve the puzzle, we use a simple simulated example to demonstrate the impact of the structural flexibility on the FSC curves.

Here, we generate simulated CryoEM density maps using the molecular model of β -galactosidase (PDB: 6CVM)²⁶. To simulate the structural flexibility, we randomize the coordinates of each atom within a local region before turning the model into a density map. This is done by shifting each atom toward a random direction for a given distance, which essentially controls the local resolution around the atom. For each of the even/odd subset, we generate 10 maps with randomized coordinates, and average them together to produce the map for the half set. Gaussian noise is added to the half maps so that the average SNR is 0.5. The “gold-standard” FSC is then computed between the results of the two half sets, without masking or other post processing steps. For two out of the four subunits of β -galactosidase, we consider them the rigid “core” of the protein and introduce only small shifts, so the local resolution is $\sim 3\text{\AA}$. For the other two subunits, we randomize the atom coordinates at different scales to simulate the impact of local structure flexibility. In the first example (blue in Fig.S5), we randomize the atom coordinates so the local resolution at the two flexible subunits is $\sim 15\text{\AA}$, whereas in the second example (red), the local resolution at the same two subunits is $\sim 7\text{\AA}$. Obviously, the two structures are essentially the same

at the two rigid subunits, and the second structure is much better resolved than the first one at the two flexible subunits. However, the first structure shows a slightly better FSC curve, despite its worse resolvability and local resolution.

A simple explanation of the phenomenon is that the real space signal at different subunits is weighted differently in the overall FSC curves, since the FSC is computed in the Fourier space. In the first structure, while the flexible subunits are poorly resolved, the average voxel intensity of the two subunits are also much lower compared to the two rigid ones, since structures of different “conformations” are averaged together. As a result, these two subunits carry a very low weight in the FSC curve, and the structure can achieve a “gold-standard” resolution of 3Å despite having half of the map only resolved at 15Å. In the second example, while the resolvability of the flexible subunits is considerably improved compared to the first structure, it is still not as good as the rigid subunits. However, the two flexible subunits now have higher voxel intensity, due to the fact that they are better resolved, thus a higher weight in the overall FSC curve. This means, the high resolution parts of the density map now weigh less in the calculation of FSC, leading to a slightly lower curve than the first example.

In summary, this simulated example suggests that the resolvability improvement of local flexible domains does not necessarily lead to the improvement of the overall FSC. To have a better measurement of the quality of a CryoEM density map, it is necessary to combine metrics including the global FSC, local resolution, local resolvability measurement such as the Q-score, as well as the real space features.

Software availability

All computational tools described here are implemented in EMAN2, a free and open source software for CryoEM/CryoET imaging processing. The code is available at github.com/cryoem/eman2, and a tutorial for these tools can be found through eman2.org/e2gmm_refine.

Data accessibility

The three data sets used in the paper are publicly available through EMPIAR. EMPIAR-10786 for the GPCR, EMPIAR-10492 for the SARS-COV2 spike, and EMPIAR-10374 for the ABC

transporter. Structures produced in this paper are deposited in EMDatabank, and the corresponding refined models in the PDB.

Acknowledgements

This research has been supported by NIH grant R21MH125285. Computational resources from SLAC Shared Scientific Data Facility (SDF) are used for the work.

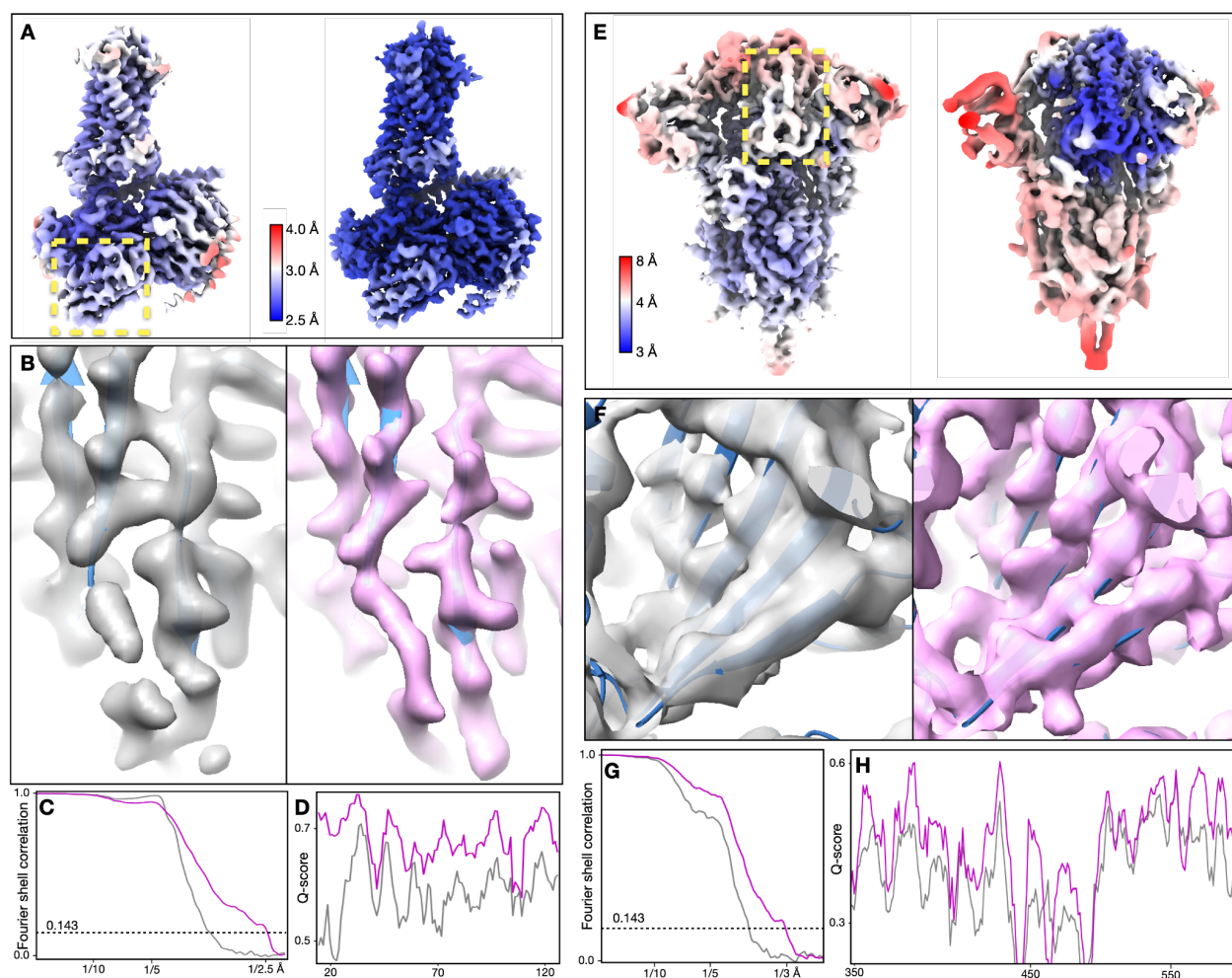


Figure 1. Refinement of GPCR (EMPIAR-10786) and SARS-COV2 spike (EMPIAR-10492) datasets. (A) Reconstructions of the GPCR using original angle assignment (left) and after the patch-by-patch alignment (right), colored by local resolution. The yellow box highlights the region shown below. (B-D) Comparison of real space features, FSC and Q-score between the original reconstruction (gray) and the patch-by-patch refinement (pink). (E) Reconstructions of the SARS-COV2 spike using original angle assignment (left) and after the focused refinement of RBD (right), colored by local resolution. The yellow box highlights the target domain for focused refinement. (F-H) Comparison of real space features, FSC and Q-score of RBD between the original reconstruction (gray) and the patch-by-patch refinement (pink).

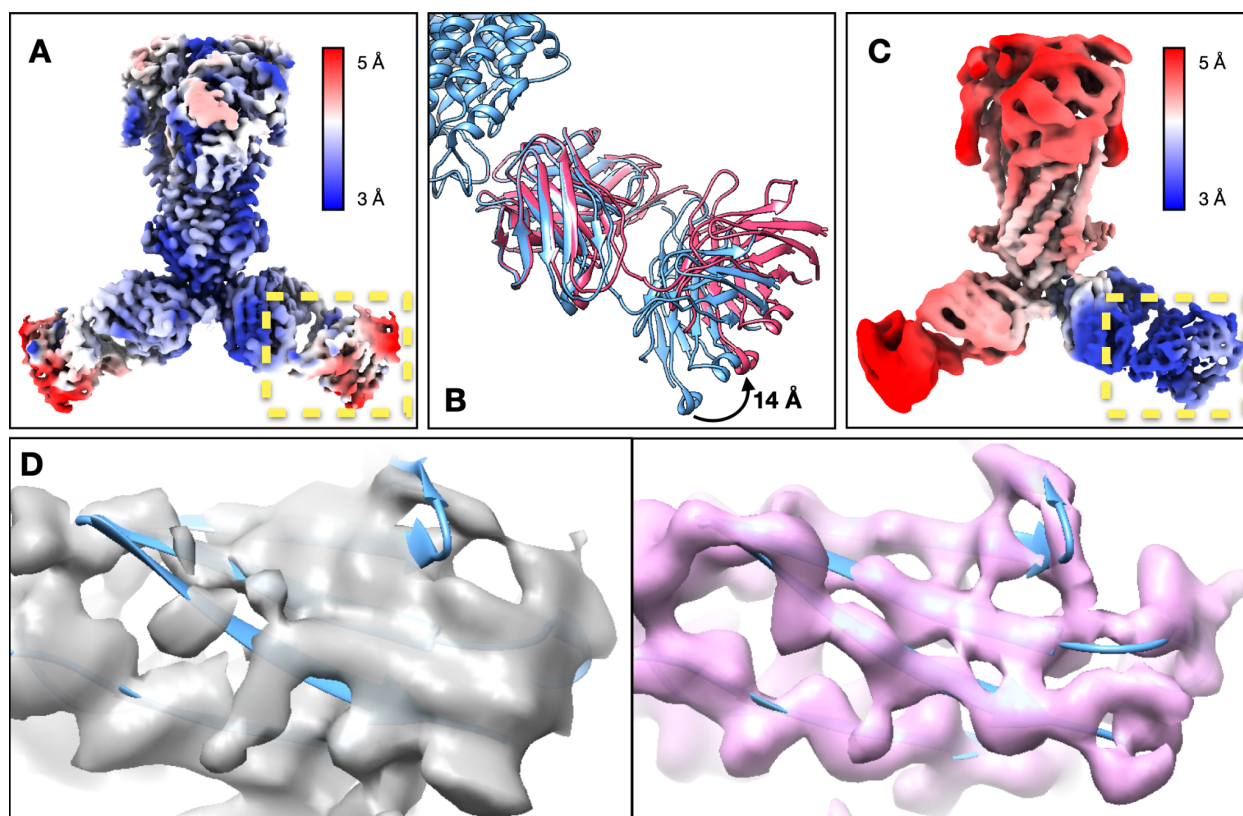


Figure 2. Refinement of the ABC transporter (EMPIAR-10374). (A) Reconstruction of the ABC transporter using original orientation assignment, colored by local resolution. (B) Continuous movement of the Fab shown in morphed molecular models. (C) Reconstruction of the ABC transporter after converting the movement trajectory to particle orientations, colored by local resolution. (D) Feature comparison at a β -sheet in the C-domain of Fab from the original structure (gray) and the structure after GMM-based refinement (pink).

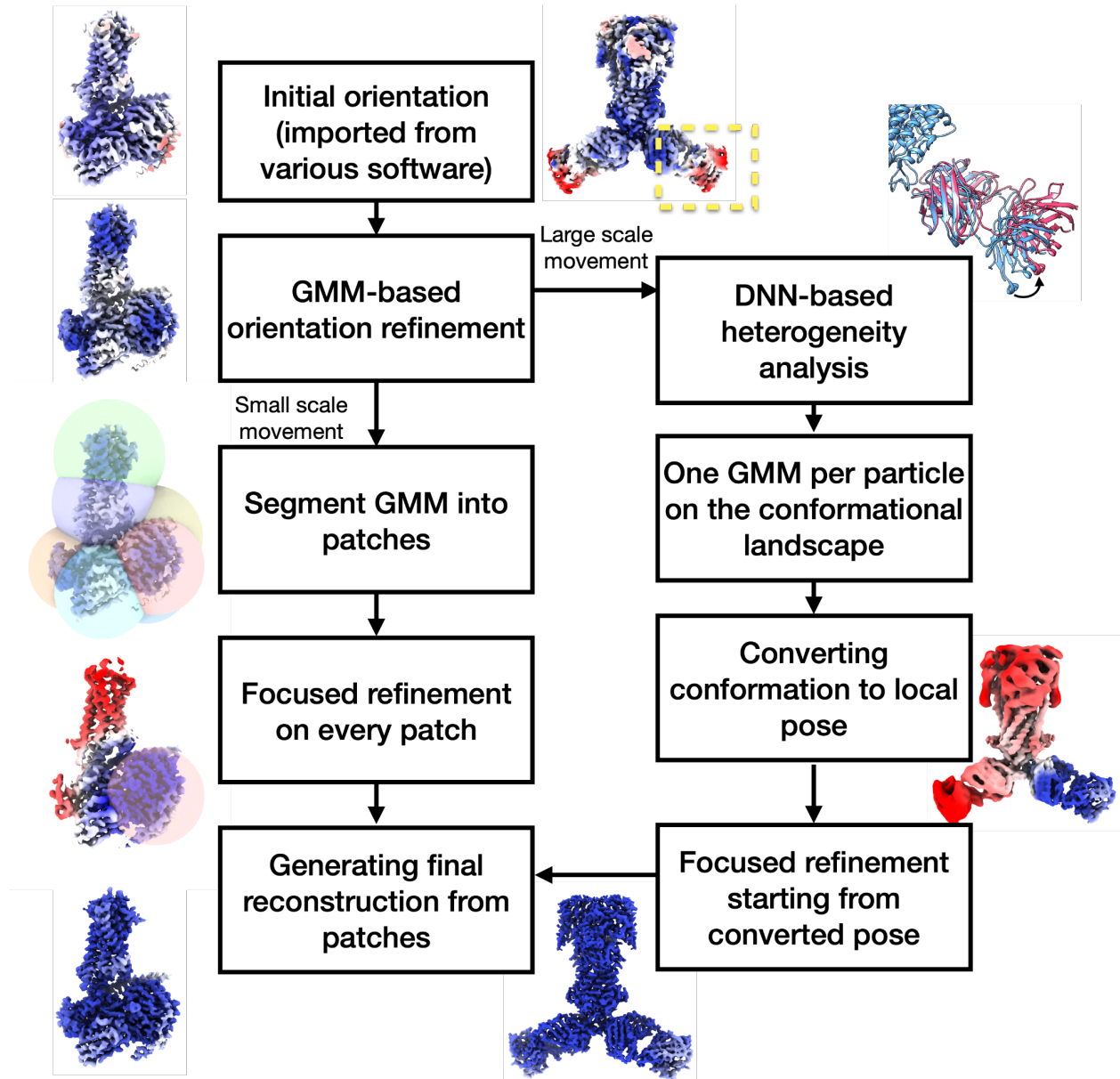


Fig S1. Workflow diagram for GMM-based particle orientation and conformation refinement.

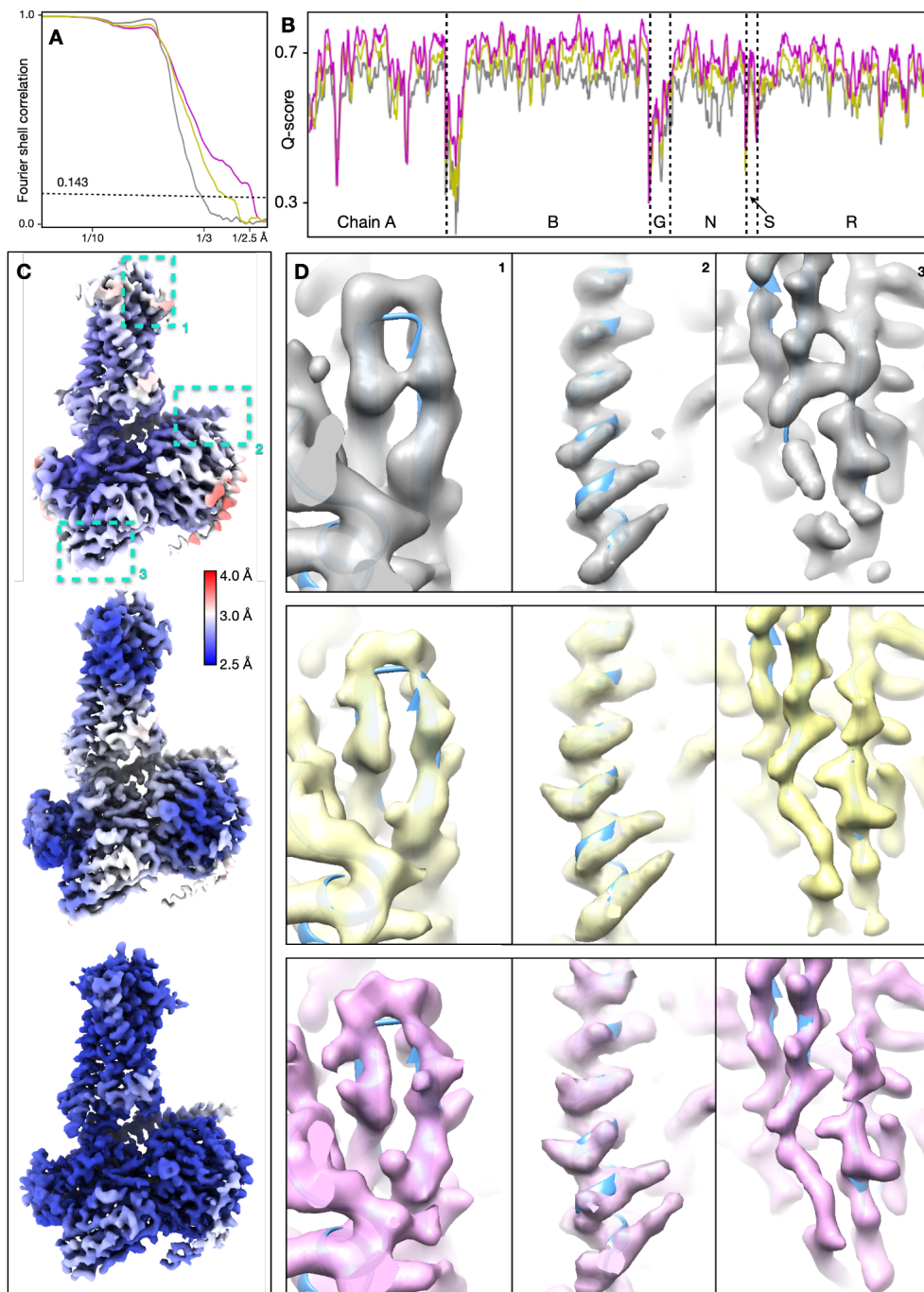


Fig S2. Detailed results of the GPCR dataset (EMPIAR-10786). (A) FSC curves of the reconstruction using initial orientation (gray), global GMM-based refinement (yellow) and patch-by-patch refinement (pink). (B) Q-score comparison of the three corresponding maps. (C-D) Overall structure of the three reconstructions, colored by local resolution, and comparison of local real space features. The cyan boxes in C highlight the location of features in the corresponding columns shown in D.

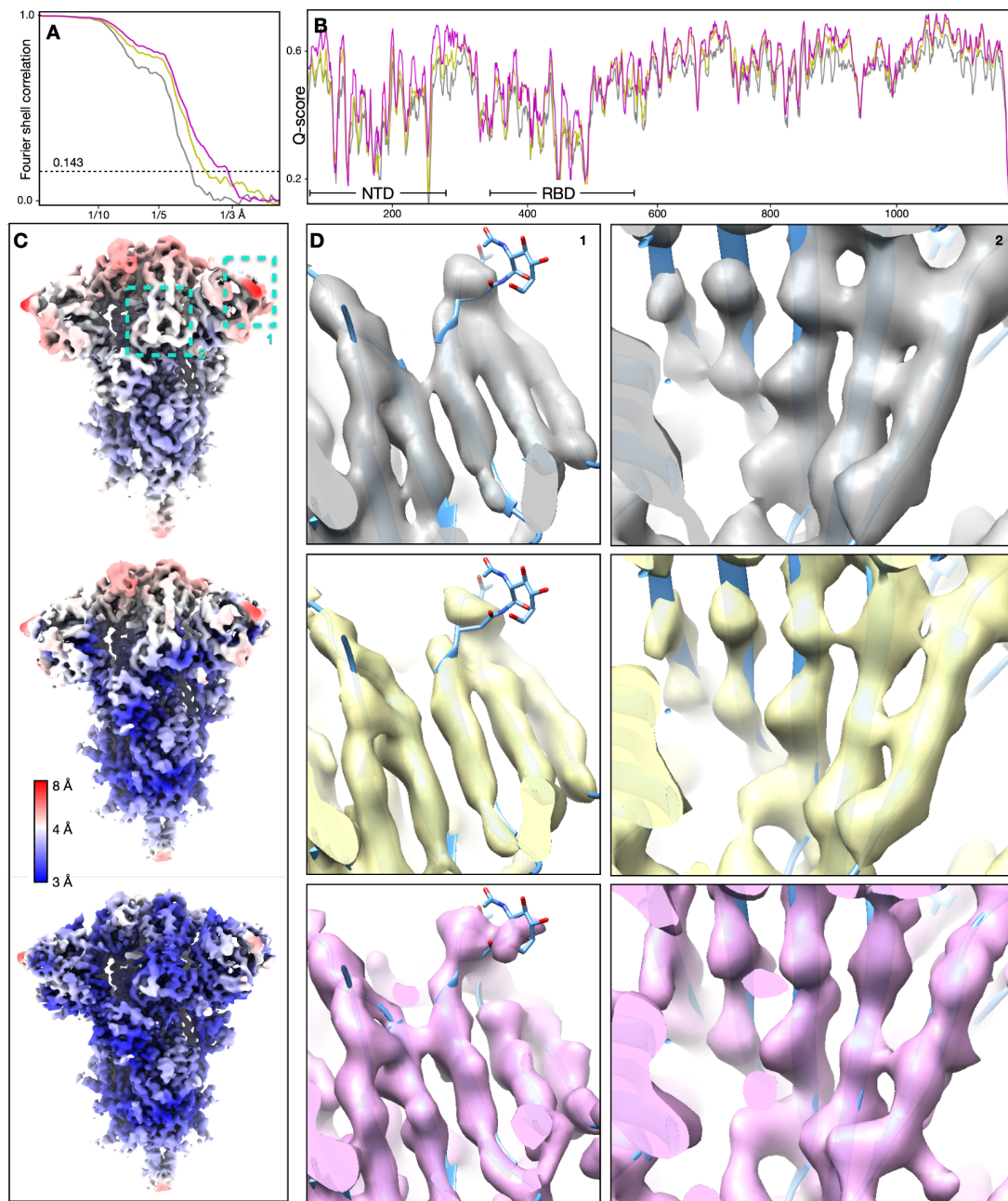


Fig S3. Detailed results of the SARS-COV2 dataset (EMPIAR-10492). (A) FSC curves of the reconstruction using initial orientation (gray), global GMM-based refinement (yellow) and patch-by-patch refinement (pink). (B) Q-score comparison of the three corresponding maps. (C-D) Overall structure of the three reconstructions, colored by local resolution, and comparison of local real space features. The cyan boxes in C highlight the location of features in the corresponding columns shown in D.

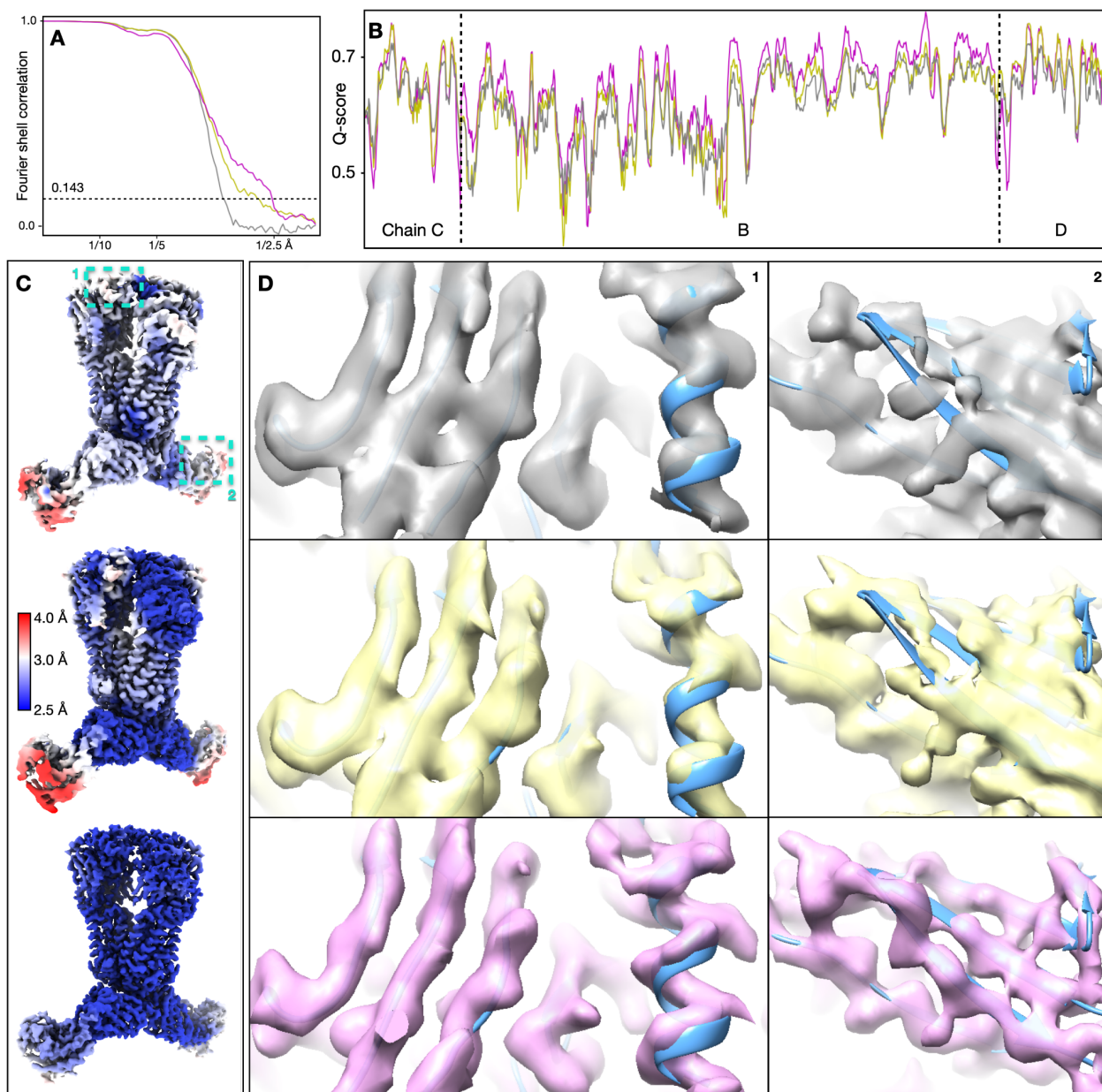


Fig S4. Detailed results of the ABC transporter dataset (EMPIAR-10374). (A) FSC curves of the reconstruction using initial orientation (gray), global GMM-based refinement (yellow) and patch-by-patch refinement (pink). (B) Q-score comparison of the three corresponding maps. (C-D) Overall structure of the three reconstructions, colored by local resolution, and comparison of local real space features. The cyan boxes in C highlight the location of features in the corresponding columns shown in D.

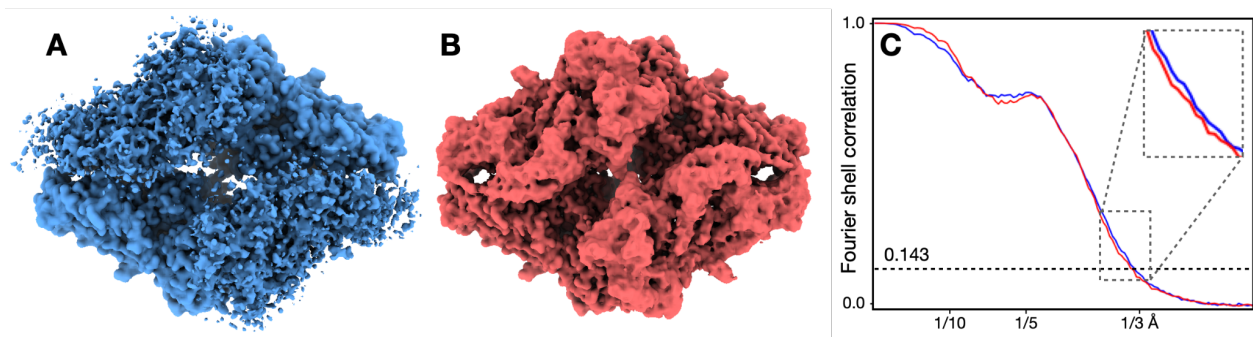


Fig S5. Impact of flexible domains on the global FSC curve. (A) Simulated density map of β -galactosidase, with two rigid subunits at 2.5Å and two flexible ones resolved at 15Å. (B) Same simulated map as A, with the two flexible subunits resolved at 7Å. (C) Comparison of “gold-standard” FSC curves of the two structures. Blue - A, red - B.

Supplementary movie 1

Structure comparison of the GPCR dataset (EMPIAR-10786). Gray: reconstruction using initial orientation. Pink: reconstruction after GMM-based patch-by-patch refinement.

Supplementary movie 2

Structure comparison of the SARS-COV2 dataset (EMPIAR-10492). Gray: reconstruction using initial orientation. Pink: reconstruction after GMM-based patch-by-patch refinement.

Supplementary movie 3

Structure comparison of the ABC transporter dataset (EMPIAR-10374). Gray: reconstruction using initial orientation. Pink: reconstruction after GMM-based patch-by-patch refinement.

Supplementary movie 4

Converting structural heterogeneity to particle orientation focusing on the Fab of the ABC transporter (EMPIAR-10374).

References

1. Cheng, Y. Single-particle cryo-EM-How did it get here and where will it go. *Science* **361**, 876–880 (2018).
2. Zhang, K., Pintilie, G. D., Li, S., Schmid, M. F. & Chiu, W. Resolving individual atoms of protein complex by cryo-electron microscopy. *Cell Res.* **30**, 1136–1139 (2020).
3. Nakane, T. *et al.* Single-particle cryo-EM at atomic resolution. *Nature* **587**, 152–156 (2020).
4. Yip, K. M., Fischer, N., Paknia, E., Chari, A. & Stark, H. Atomic-resolution protein structure determination by cryo-EM. *Nature* **587**, 157–161 (2020).
5. Scheres, S. H. W. RELION: implementation of a Bayesian approach to cryo-EM structure determination. *J. Struct. Biol.* **180**, 519–530 (2012).
6. Tang, G. *et al.* EMAN2: an extensible image processing suite for electron microscopy. *J. Struct. Biol.* **157**, 38–46 (2007).
7. Nakane, T., Kimanius, D., Lindahl, E. & Scheres, S. H. Characterisation of molecular motions in cryo-EM single-particle data by multi-body refinement in RELION. *Elife* **7**, (2018).
8. Zhong, E. D., Bepler, T., Berger, B. & Davis, J. H. CryoDRGN: reconstruction of heterogeneous cryo-EM structures using neural networks. *Nat. Methods* **18**, 176–185 (2021).
9. Punjani, A. & Fleet, D. J. 3D variability analysis: Resolving continuous flexibility and discrete heterogeneity from single particle cryo-EM. *J. Struct. Biol.* **213**, 107702 (2021).
10. Punjani, A. & Fleet, D. J. 3D Flexible Refinement: Structure and Motion of Flexible Proteins from Cryo-EM. *bioRxiv* 2021.04.22.440893 (2021) doi:10.1101/2021.04.22.440893.
11. Herreros, D. *et al.* Estimating conformational landscapes from Cryo-EM particles by 3D Zernike polynomials. *Nat. Commun.* **14**, 154 (2023).
12. Chen, M. & Ludtke, S. J. Deep learning-based mixed-dimensional Gaussian mixture model for characterizing variability in cryo-EM. *Nat. Methods* **18**, 930–936 (2021).

13. Punjani, A., Rubinstein, J. L., Fleet, D. J. & Brubaker, M. A. cryoSPARC: algorithms for rapid unsupervised cryo-EM structure determination. *Nat. Methods* **14**, 290–296 (2017).
14. Kingma, D. P. & Ba, J. Adam: A Method for Stochastic Optimization. *arXiv [cs.LG]* (2014).
15. Chen, M., Toader, B. & Lederman, R. Integrating Molecular Models Into CryoEM Heterogeneity Analysis Using Scalable High-resolution Deep Gaussian Mixture Models. *J. Mol. Biol.* 168014 (2023).
16. Martín~Abadi *et al.* TensorFlow: Large-Scale Machine Learning on Heterogeneous Systems. Preprint at (2015).
17. Harris, J. A. *et al.* Selective G protein signaling driven by substance P-neurokinin receptor dynamics. *Nat. Chem. Biol.* **18**, 109–115 (2022).
18. Pintilie, G. *et al.* Measurement of atom resolvability in cryo-EM maps with Q-scores. *Nat. Methods* **17**, 328–334 (2020).
19. Ke, Z. *et al.* Structures and distributions of SARS-CoV-2 spike proteins on intact virions. *Nature* **588**, 498–502 (2020).
20. Jackson, S. M. *et al.* Structural basis of small-molecule inhibition of human multidrug transporter ABCG2. *Nat. Struct. Mol. Biol.* **25**, 333–340 (2018).
21. Asarnow, D., Palovcak, E. & Cheng, Y. *asarnow/pyem: UCSF pyem v0.5.* (2019). doi:10.5281/zenodo.3576630.
22. Penczek, P. A. Reliable cryo-EM resolution estimation with modified Fourier shell correlation. *IUCrJ* **7**, 995–1008 (2020).
23. Afonine, P. V. *et al.* Real-space refinement in PHENIX for cryo-EM and crystallography. *Acta Crystallogr D Struct Biol* **74**, 531–544 (2018).
24. Pettersen, E. F. *et al.* UCSF Chimera--a visualization system for exploratory research and analysis. *J. Comput. Chem.* **25**, 1605–1612 (2004).
25. Goddard, T. D. *et al.* UCSF ChimeraX: Meeting modern challenges in visualization and analysis. *Protein Sci.* **27**, 14–25 (2018).

26. Bartesaghi, A. *et al.* Atomic Resolution Cryo-EM Structure of β -Galactosidase. *Structure* **26**, 848-856.e3 (2018).